JACS
JOURNAL OF THE AMERICAN CHEMICAL SOCIETY

Article

Keto-enol tautomerization triggers an electrophilic aldehyde deformylation reaction by a nonheme manganese(III)-peroxo complex

Fabián G. Cantú Reinhard, PRASENJIT BARMAN, Gourab Mukherjee, Jitendra Kumar, Deep Kumar, Devesh Kumar, chivukula V. sastri, and Sam P. de Visser

J. Am. Chem. Soc., **Just Accepted Manuscript** • DOI: 10.1021/jacs.7b10033 • Publication Date (Web): 17 Nov 2017

ACS Publications

Journal of the American Chemical Society is published by the American Chemical Society. 1155 Sixteenth Street N.W., Washington, DC 20036

Keto-enol tautomerization triggers an electrophilic aldehyde deformylation reaction by a nonheme manganese(III)-peroxo complex.

Fabián G. Cantú Reinhard,‡ Prasenjit Barman,⊥ Gourab Mukherjee,⊥ Jitendra Kumar,§ Deep Kumar,§ Devesh Kumar,§ Chivukula V. Sastri*,⊥ and Sam P. de Visser*,‡

‡ The Manchester Institute of Biotechnology and School of Chemical Engineering and Analytical Science, The University of Manchester, 131 Princess Street, Manchester M1 7DN, United Kingdom

⊥ Department of Chemistry, Indian Institute of Technology Guwahati 781039, Assam, India

§ Department of Applied Physics, School of Physical Sciences, Babasaheb Bhimrao Ambedkar University, Lucknow 226025, UP, India

ABSTRACT: Oxygen atom transfer by high-valent enzymatic intermediates remains an enigma in chemical catalysis. In particular, manganese is an important first-row metal involved in key biochemical processes including the biosynthesis of molecular oxygen (through the photosystem II complex) and biodegradation of toxic superoxide to hydrogen peroxide by superoxide dismutase. Biomimetic models of these biological systems have been developed to gain understanding on the structure and properties of short-lived intermediates but also with the aim to create environmentally benign oxidants. In this work, we report a combined spectroscopy, mass spectrometry, kinetics and computational study on aldehyde deformylation by two side-on manganese(III)-peroxo complexes with bispidine ligands. Both manganese(III)-peroxo complexes are characterized by UV-Vis and mass spectrometry techniques and their reactivity patterns with aldehydes was investigated. We find a novel mechanism for the reaction that is initiated by a hydrogen atom abstraction reaction, which enables a keto-enol tautomerization in the substrate. This is an essential step in the mechanism that makes an electrophilic attack on the olefin bond possible as the attack on the aldehyde carbonyl is too high in energy. Kinetics studies determine a large kinetic isotope effect for the replacement of the transferring hydrogen atom by deuterium, while replacing the transferring hydrogen atom by a methyl group makes the substrate inactive and hence confirm the hypothesized mechanism. Our new mechanism is confirmed with density functional theory modelling on the full mechanism and rationalized through valence bond and thermochemical cycles. Our unprecedented new mechanism may have relevance to biological and biomimetic chemistry processes in general and gives insight in metal-peroxo and metal-hydroperoxo intermediates in general.

Introduction.

Metalloenzymes are powerful oxidants in nature that catalyze important reactions for Biosystems.[1] Most of these metalloenzymes utilize iron as their central co-factor, due to its high natural abundance. Another transition metal in relatively large abundance in the Earth Crust is manganese and, as such, Nature has found key uses of it in various biological transformations.[2] Thus, manganese complexes are strong oxidizers and consequently, the active site of superoxide dismutase (SOD) contains a central Mn atom.[3] SOD is involved in the biodegradation of superoxide radicals and converts them on a manganese center to hydrogen peroxide. Often SOD enzymes are anchored to a catalase enzyme that react and detoxify hydrogen peroxide. Another biological system with manganese coordination is the Photosystem II (PSII) active cluster, which contains four manganese atoms held together with bridging oxygen atoms and a dangling Ca^{2+} ion in a cubane-type Mn_4O_5Ca cluster.[4] This cluster binds water molecules and reacts them to one molecule of molecular oxygen with the release of four protons.

In biomimetic chemistry, synthetic manganese containing models of SOD and PSII have been created and studied for their chemical properties and reactivity.[5]

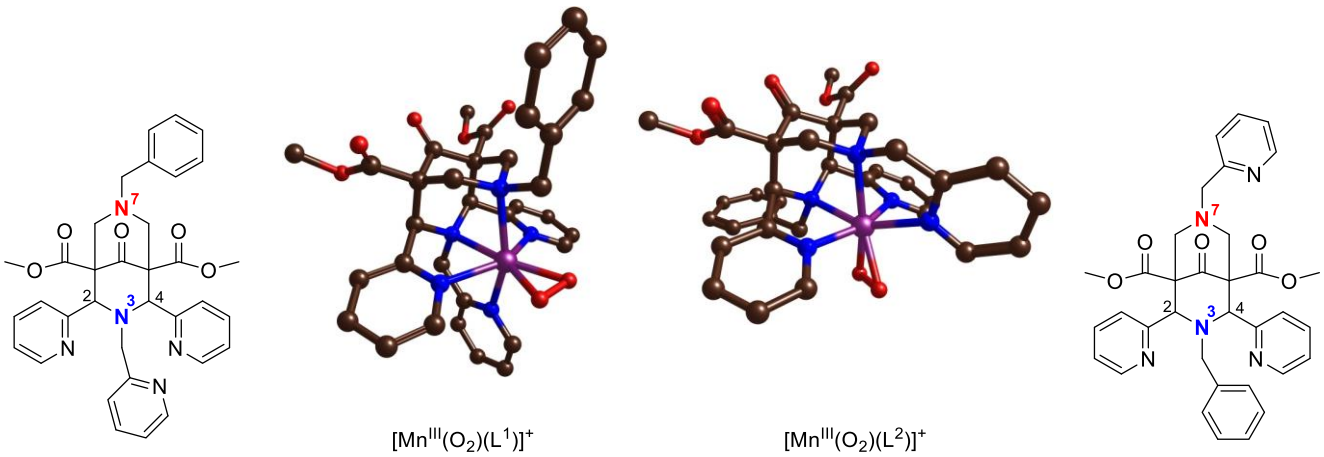

Figure 1. Manganese(III)-peroxo complexes investigated in this work.

In several of these studies a manganese-peroxo was investigated and the spectroscopic features of the complexes was established with UV-Vis, resonance Raman, infrared absorption, and electron paramagnetic resonance (EPR) spectroscopy.[6,7] Furthermore, the reactivity of manganese-peroxo with respect to substrates was investigated and efficient conversion to aldehydes into deformylation products was obtained.[8] However, the exact details of the mechanism remain a mystery. Therefore, manganese(III)-peroxo shows interesting reactivity patterns with substrates that are still poorly understood.

Recently, our groups have shown that bispidine ligated manganese(III)-peroxo reacts with aldehydes through a rate determining hydrogen atom abstraction reaction as evidenced from a large kinetic isotope effect (KIE) for the replacement of the α-hydrogen atom by deuterium.[9] Radical trapping experiments and density functional theory calculations further confirmed the rate determining hydrogen atom abstraction and rationalized that this is originating from a more feasible electron transfer from peroxo to Mn as compared to substrate carbonyl. The question, therefore, is how the ligand system of the metal influences the bifurcation pathways between hydrogen atom abstraction, i.e. the electrophilic pathway, versus nucleophilic pathways.

To test the ligand effect on the bifurcation pathways we followed our study up with a detailed study on two functionally isomeric pentadentate manganese(III)-peroxo complexes resulting in different orientations of two pyridine groups with respect to N^3 nitrogen of the bispidine back-bone. In particular, we synthesized manganese(III)-peroxo complexes with bispidine ligand systems (see Figure 1), namely $[Mn^{III}(O_2)(L^1)]^+$ (**1**) and $[Mn^{III}(O_2)(L^2)]^+$ (**2**) with L^1 = dimethyl-2,4-di(2-pyridyl)3-(pyridin-2-ylmethyl)-7-benzyl-3,7-diaza-bicyclo[3.3.1] nonan-9-one-1,5-dicarboxylate) and L^2 = dimethyl 2,4-di(2-pyridyl)-3-benzyl-7-(pyridin-2-ylmethyl)-3,7-diazabicyclo[3.3.1] nonan-9-one-1,5-dicarboxylate). Thus ligand L^1 has three pyridine groups pointing upwards, i.e. along the molecular *z*-axis with the ortho-C–H groups in hydrogen bonding distance to the sixth ligand, whereas in ligand L^2 only one of those points upwards and the other two are aligned with the *xy*-plane. Our combined experimental and computational study gives evidence of a novel reaction mechanism starting with a rate determining hydrogen atom abstraction reaction and followed by a reshuttle of the hydrogen atom through a keto-enol tautomerization to set up a low energy nucleophilic attack of peroxo on an olefin bond of the substrate. Alternative reaction mechanisms were tested and ruled out. Our observations are confirmed with computational modelling that rationalized the reaction mechanism with valence bond and thermochemical cycles.

Methods.

Experimental procedures. Our procedures are similar to previous studies of our groups and will be summarized briefly here.[10] All reagents were obtained from Aldrich Chemical Co., and obtained at the best available purity and used without further purification unless otherwise indicated. Solvents were dried according to published procedures and distilled under argon prior to use.[11] The piperidone backbone of the ligands L^1 and L^2 were prepared according to a literature protocol,[12] and used to generate the $[Mn^{II}(L^1)](ClO_4)_2$ and $[Mn^{II}(L^2)](ClO_4)_2$ complexes. Subsequently, the manganese(III)-peroxo complexes were prepared by reacting their corresponding Mn^{II} systems with 10 equiv. of H_2O_2 and 2.5 equiv. triethylamine (TEA) in acetonitrile (2 mL) at 15°C.

2-Methyl-2-phenylpropionaldehyde (2-Me-PPA) was synthesized in our laboratory according to a literature procedure,[13] while α-[D_1]-2-phenylpropionaldehyde (α-[D_1]-PPA, ~90%, D enriched) was purchased from RVL Scientific & Engineering Pvt. Ltd. (Lucknow, India) and the purity of the compound was confirmed by NMR. All NMR spectra were recorded in $CDCl_3$.

Syntheses and characterization. Bispidine ligands (0.17 mmol) were dissolved in acetonitrile and mixed with $Mn^{II}(ClO_4)_2$•$2CH_3CN$ salt (0.22 mmol in CH_3CN) under inert conditions. The pale yellow solution was refluxed over-

night and filtered through a 0.2 micron syringe filter and layered with ether to obtain a white crystal suitable for X-ray diffraction. The cif file of the complexes is deposited at the Cambridge Crystallographic Data Centre (CCDC) with the following deposition numbers CCDC 1022749 and 1022750. *Caution! Metal perchlorate salts are potentially explosive and should be handled with excessive care.*

Instrumentation. NMR (^{1}H and ^{13}C) spectra were recorded with a Bruker 600/150 MHz spectrometer. UV-Vis spectra and kinetic measurements were performed with a Hewlett Packard 8453 spectrophotometer equipped with either a constant temperature circulating water bath or a liquid nitrogen cryostat (Unisoku) with a temperature controller. High Resolution electrospray ionization mass spectra (ESI-MS) of $[Mn^{III}(O_2)(L^1)]^+$ and $[Mn^{III}(O_2)(L^2)]^+$ were recorded on a Waters (Micromass MS Technologies) Q-TOF Premier mass spectrometer by infusing pre-cooled samples directly into the source at 15 μL min^{-1} using a syringe pump. The spray voltage was set at 2 kV and the capillary temperature at 80°C.

Reactivity Studies. The chemical reactions were monitored in a 10 mm path length cuvette by measuring the UV-Vis spectral changes of the reaction solutions as a function of time. The rate constants were determined by fitting the changes in absorbance of the intermediates under study. The rate constants were averaged from three individual experiments, and resulted in a standard deviation of less than 10% of the given values.

Product Analysis. Product analysis was performed on a WATERS ACQUITY UPLC equipped with a variable wavelength UV-200 detector. Products were separated on a Waters Symmetry C18 reverse phase column (4.6 × 250 mm), and detection was made at 215 and 254 nm and product yields were determined by comparison with standard curves of known authentic samples. All experiments were done at least in triplicate.

Computational procedures. Density functional theory (DFT) calculations were performed on the catalytic reaction mechanism of deformylation of 2-phenylpropionaldehyde (2-PPA) by $[Mn^{III}(O_2)(L^1)]^+$ and $[Mn^{III}(O_2)(L^2)]^+$ following previously tested and benchmarked procedures.[14] We took initial structures from our previous study,[9] but reoptimized all geometries in Gaussian-09 with a full solvent model as mimicked by a the polarized continuum model (PCM) with a dielectric constant of 37.5 mimicking acetonitrile.[15,16] These geometry optimizations utilized the unrestricted B3LYP hybrid density functional method in combination with an LACVP basis set with core potential on Mn and 6-31G* on the rest of the atoms (basis set BS1).[17,18] The nature of the stationary points was confirmed through a frequency calculation also under solution conditions calculated with the PCM model. All local minima had real frequencies only, while the transition states were characterized by a single imaginary mode for the correct transition. To improve the energetics, single point calculations using an LACV3P+ basis set with core potential on Mn and 6-311+G* on the rest of the atoms was performed: Basis set BS2. Previously, we showed that little changes in structure and energetics are obtained for UB3LYP/BS1 versus UB3LYP/BS2 geometry optimizations.[19] Furthermore, the spin state ordering and relative energies of related manganese complexes were tested using a range of alternative DFT and ab initio methods.[20] Based on the fact that manganese(III)-peroxo has a high-spin state ground state, we selected B3LYP as computational method and the results reproduce the experimental trends well.

Kinetic isotope effects (KIE) were evaluated computationally by reevaluating the free energy and vibrational frequencies of the structures, whereby one or more hydrogen atom is replaced by deuterium.[21] The Eyring kinetic isotope effect (KIE_{Eyring}) is determined from the change in free energy of activation ($\Delta G^{\ddagger}$) between the system with hydrogen and deuterium atoms, Eq 1, with R representing the gas constant and T the temperature (298K).

$$KIE_{Eyring} = \exp\{(\Delta G^{\ddagger}_{D} - \Delta G^{\ddagger}_{H})/RT\} \quad (1)$$

In addition, we estimated the Wigner kinetic isotope effect (KIE_{Wigner}), which corrects KIE_{Eyring} with tunneling corrections Q_t for the hydrogen and deuterium reactions through Eq 2 and 3. These equations contain Planck's constant (h), Boltzmann's constant (k_B) and the imaginary frequency in the transition state (ν).

$$KIE_{Wigner} = KIE_{Eyring} \times Q_{t,H}/Q_{t,D} \quad (2)$$

$$Q_t = 1 + (h\nu/k_BT)^2/24 \quad (3)$$

Results.

In this work we describe the synthesis, characterization and reactivity patterns of two novel side-on manganese(III)-peroxo complexes with a pentadentate bispidine N5 ligand, i.e. $[Mn^{III}(O_2)(L^1)]^+$ (**1**) and $[Mn^{III}(O_2)(L^2)]^+$ (**2**), Figure 1. These two ligand systems have their equatorial pyridine groups either axial or equatorial to the manganese(III)-peroxo group and, hence interact differently with an approaching substrate. The weak intermolecular interactions separating the two complexes may incur functional differences due to the way substrate can approach to the catalytic center and/or the stability of the reactant complex. Therefore, these models may give insight into the properties and functions of enzymatic catalysts where substrate approach is often tightly controlled.[22]

Upon addition of 10 equiv. of H_2O_2 to $[Mn^{II}(L^2)(ClO_4)_2]^{2+}$ in the presence of 2.5 equiv. of TEA a brown intermediate is formed with distinctive absorption features, Figure S2. The ESI mass spectra of **1** and **2** exhibit prominent peaks with *m/z* 678 and an isotope pattern that identify them as $[Mn^{III}(O_2)(L^1)]^+$ and $[Mn^{III}(O_2)(L^2)]^+$. When $H_2{}^{16}O_2$ was replaced by $H_2{}^{18}O_2$ in the reaction mixture, the mass of the parent ion increased with four units indicative of a dioxygen-bound complex. We attempted to resolve the resonance Raman spectrum of **1** and **2**, but due to degradation of the manganese complexes caused by scattering all our efforts failed.

Subsequently, we investigated the deformylation behavior of compounds **1** and **2** in a reaction with 2-phenylpropionaldehyde (2-PPA). This was done by monitoring the change in UV-Vis absorption spectra as a function of time after the addition of substrate. In particular, the aldehyde deformylation reaction and the mechanism of substrate activation by side-on manganese(III)-peroxo was investigated from the reactivity of $[Mn^{III}(O_2)(L^1)]^+$ and $[Mn^{III}(O_2)(L^2)]^+$ with 2-PPA under the same experimental reaction conditions (Figure 2). Addition of 2-PPA to **2** in acetonitrile at 15°C led to immediate decay of the intermediate and the formation of acetophenone product as identified by NMR. The pseudo first-order rate constant for the decay of **2** increased linearly with increasing concentration of 2-PPA, and enabled us to measure the second-order rate constant: $k_2 = 1.42 \times 10^{-1}$ M^{-1} s^{-1}. For comparison, the second-order rate constant for the reaction of $[Mn^{III}(O_2)(L^1)]^+$ with 2-PPA was 2.74×10^{-2} M^{-1} s^{-1}.[9] Therefore, it appears that $[Mn^{III}(O_2)(L^2)]^+$ reacts with 2-PPA about five times faster than the isomeric oxidant with ligand L^1. These results were in fact in opposite trend to those obtained in the reactivity of the corresponding manganese(IV)-oxo complexes $[Mn^{IV}(O)(L^1)]^{2+}$ and $[Mn^{IV}(O)(L^2)]^{2+}$.[12d] A possible reason for the change in rate constant ordering is the shape of the ligand system, whereby the L^1 ligand (see Figure 1) has protons pointing upwards toward the peroxo group, whereas in the L^2 ligand the pyridine moieties are in the *xy*-plane and will not interact with the approaching substrate.

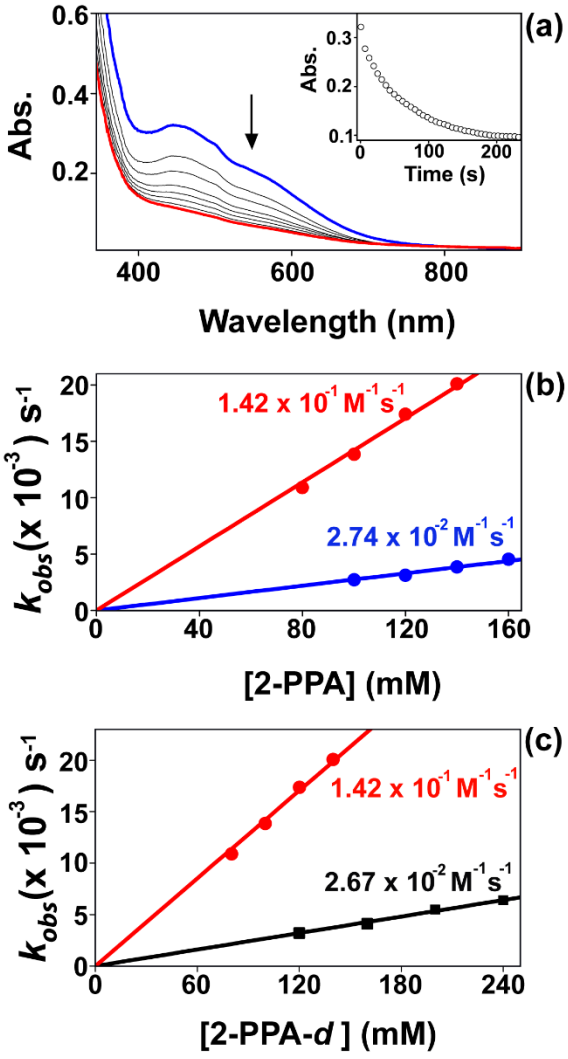

Figure 2. Kinetics of the reaction of **2** with 2-PPA. (a) UV-Vis spectral changes of **2** (2 mM) upon addition of 2-PPA (120 mM) in the presence of TEA (5 mM) and hydrogen peroxide (20 mM) in CH_3CN at 15°C. The inset shows the time course of the absorbance at 450 nm. (b) Plot of k_{obs} against the concentration of 2-PPA and the derived second-order rate constant for the reaction of 2 mM **1** and **2** with 2-PPA at various concentrations in CH_3CN at 15°C [data for **2** (red •) and **1** (blue •) are given]. (c) Plot of k_{obs} against the concentration of α-[D_1]-PPA (~90%, D enriched, ■) with **2** in CH_3CN at 15°C.

To understand the details of the rate determining step for the reaction of $[Mn^{III}(O_2)(L^1)]^+$ and $[Mn^{III}(O_2)(L^2)]^+$ with 2-PPA, we decided to investigate the kinetic isotope effect (KIE) for replacing the α-hydrogen atom with deuterium (Figure 2c). Thus, upon addition of α-[D_1]-PPA (~90%, D-enriched) to **2** in acetonitrile at 15°C the absorption of the intermediates shows decay from which we determined a second-order rate constant of $k_2 = 2.67 \times 10^{-2}$ M^{-1} s^{-1}. Hence, the reaction between **2** and 2-PPA proceeds with a KIE = 5.3 and it can be concluded that the reaction has a

rate determining hydrogen atom abstraction step. A comparable KIE value of 5.4 was determined for the reactivity difference of **1** with 2-PPA/α-[D_1]-PPA.[9] Consequently, both $[Mn^{III}(O_2)(L^1)]^+$ and $[Mn^{III}(O_2)(L^2)]^+$ react with 2-PPA through a rate determining hydrogen atom abstraction and a KIE that deviates from unity and most likely their reaction mechanisms will be similar.

To further ascertain that hydrogen atom abstraction from the α-position is key to the reaction mechanism, we used a mechanistic probe, namely 2-methyl-2-phenyl propionaldehyde (2-Me-PPA), Scheme 1. Lack of reactivity with this probe would confirm that the rate determining step is indeed α-hydrogen atom abstraction and no nucleophilic pathway is possible. When we add 2-Me-PPA to **2** at 15°C, however, no reaction products are observed and only natural decay profiles back to $[Mn^{II}(L^2)]^{2+}$ are seen due to the short lifetime of the parent complex in solution ($t_{1/2}$ ~ 45 min). After analyzing the reaction solution with ESI-MS we do not find any evidence of deformylated products. Consequently, the reactivity study with 2-Me-PPA as a mechanistic probe confirms that the reaction of **2** with 2-PPA does not proceed through a rate determining nucleophilic attack on the carbonyl group but is initiated by activation of the α-hydrogen atom instead.

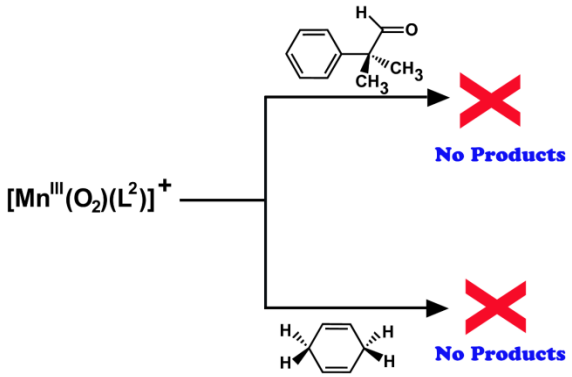

Scheme 1. Reaction of $[Mn^{III}(O_2)(L^2)]^+$ with substrates.

To test whether the manganese(III)-peroxo can react efficiently through hydrogen atom abstraction, we decided to test alternative substrates with weak C–H bonds. Addition of 1,4-cyclohexadiene to either **1** or **2** did not lead to decay of the spectroscopic features of the manganese(III)-peroxo structures, Scheme 1, hence $[Mn^{III}(O_2)(L^1)]^+$ and $[Mn^{III}(O_2)(L^2)]^+$ are unable to react via desaturation pathways. This is surprising as the deformylation reaction described above appears to have a rate determining hydrogen atom abstraction step from 2-PPA to $[Mn^{III}(O_2)(L^2)]^+$. Moreover, the mechanistic probes ruled out the more commonly seen nucleophilic attack on the carbonyl group. Computational modelling, vide infra, established the reasons behind the lack of reactivity towards cyclohexadiene as resulting from an energetically high second hydrogen atom abstraction.

Finally, a radical trapping experiment with bromotrichloromethane was performed to establish that the reaction mechanism of manganese(III)-peroxo with aldehydes proceeds through a radical intermediate species.[9,23] Addition of 2-PPA to intermediate **2** in the presence of excess $CBrCl_3$ or CBr_4 in acetonitrile at 15°C, leads to the formation of α-brominated product of the 2-PPA exclusively, Scheme 2, which was confirmed by NMR analysis (see Supporting Information, Figure S4). Consequently, our radical trapping experiment confirms a radical mechanism that most likely starts with hydrogen atom abstraction from the α-position of 2-PPA.

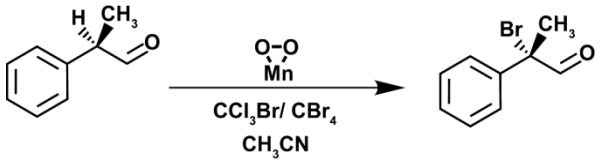

Scheme 2. Reaction of $[Mn^{III}(O_2)(L^2)]^+$ with radical trapping substrates.

In conclusion, experimental kinetics studies find that aldehyde deformylation starts with a rate determining hydrogen atom abstraction from the α-position of 2-PPA leading to a radical intermediate. On the other hand, no reactivity is observed between $[Mn^{III}(O_2)(L^2)]^+$ and substrates with weak C–H bonds such as cyclohexadiene. To understand the reaction mechanisms and explain the reactivity patterns of side-on manganese(III)-peroxo with substrates, a computational study was performed.

Computational modelling. To explain the experimentally obtained results on the reactivity of side-on manganese(III)-peroxo with aldehydes, we embarked on a density functional theory study on the possible reaction mechanisms leading to aldehyde deformylation by these complexes. Although we tested many possible mechanisms and spin states (vide infra), our lowest energy pathway leading to the first oxygen atom transfer is on a quintet spin state, Figure 3. The reaction starts with a hydrogen atom abstraction via transition state $\mathbf{TS}_{HAT1}$ and forms a manganese(II)-hydroperoxo with a radical intermediate $\mathbf{I}_1$.

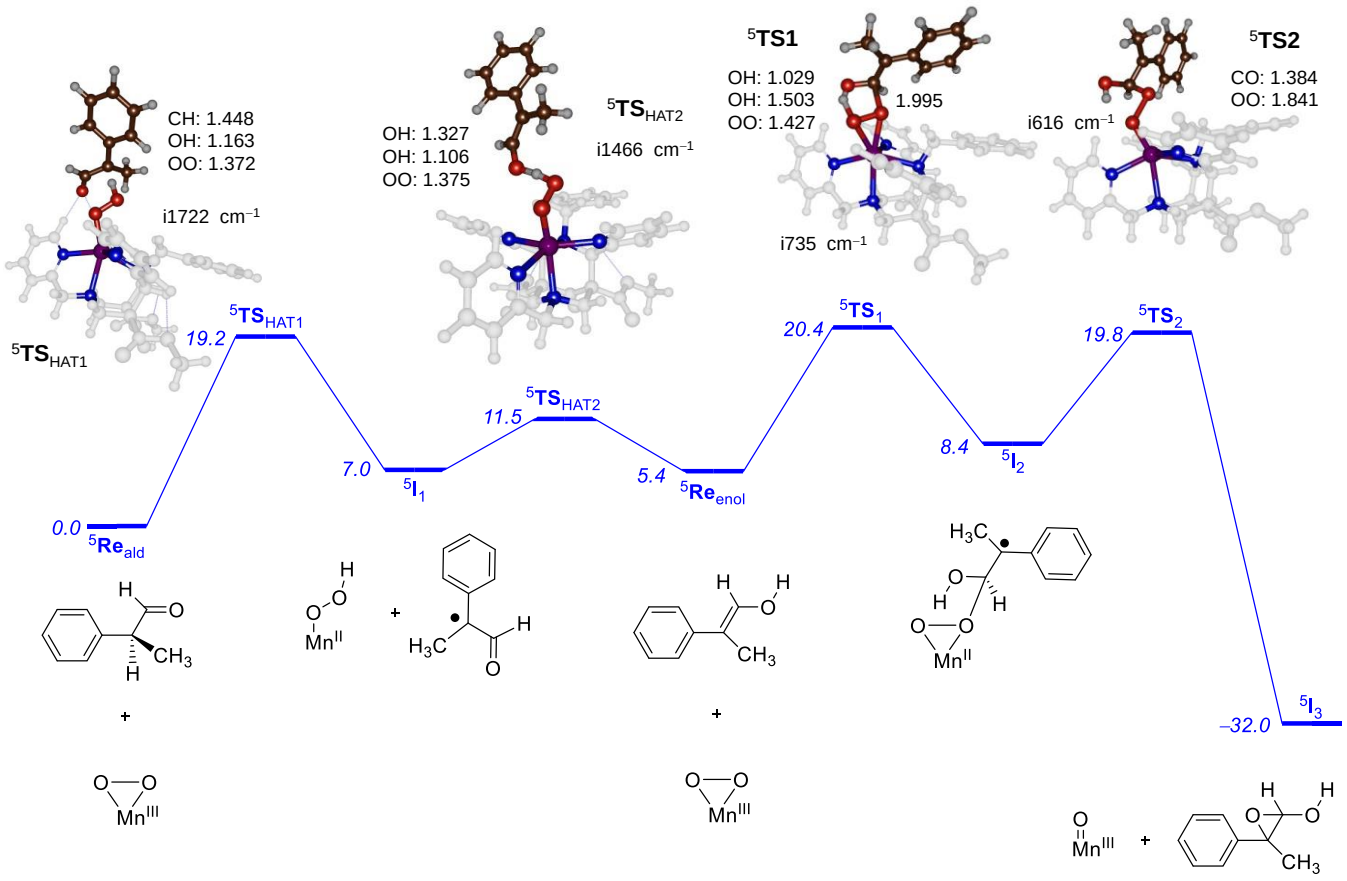

Figure 3. Potential energy profile (UB3LYP/BS2//UB3LYP/BS1+ZPE) for oxygen atom transfer from $[Mn^{III}(O_2)(L^2)]^+$ to 2-PPA with energies in kcal mol^{-1}. Transition state structures give distances in angstroms and the imaginary frequency in cm^{-1}.

In the quintet spin state the barrier is 19.2 kcal mol^{-1} and the reaction is endothermic by 7.0 kcal mol^{-1}.

Rather than radical rebound, however, as is common in typical hydrogen atom abstraction reactions,[24] actually the hydrogen atom is bounced back to substrate to give the enol form of substrate and manganese(III)-peroxo via a subsequent barrier **TS**$_{HAT2}$ of 4.5 kcal mol^{-1}. The enol form of the reactant (^{5}**Re**$_{enol}$) is slightly lesser stable than the keto form (by 5.4 kcal mol^{-1}). Once the reactant is in the enol-form, the manganese(III)-peroxo part of the reactant complex attacks the substrate olefin bond via a nucleophilic transition state ^{5}**TS1** of 20.4 kcal mol^{-1} to form the radical intermediate ^{5}**I**$_2$. Energetically, ^{5}**I**$_2$ is close in energy to ^{5}**I**$_1$ and ^{5}**Re**$_{enol}$ and will react via an O–O cleavage barrier (^{5}**TS2**) to form a manganese(III)-oxo complex and an epoxide (^{5}**I**$_3$) in a highly exothermic process. As such, the computational studies implicate that probably the first steps in the reaction mechanism will be reversible, but the step from ^{5}**I**$_2$ to ^{5}**I**$_3$ will be irreversible. We also tested the triplet spin pathway, but found it at least 20 kcal mol^{-1} higher in energy along the full profile (see Supporting Information).

Geometrically, ^{5}**TS**$_{HAT1}$ and ^{5}**TS**$_{HAT2}$ have features typical of hydrogen atom abstraction barriers seen before for the reaction of heme and nonheme iron(IV)-oxo with aliphatic substrates.[25] Both barriers have a large imaginary frequency, which implies that substitution of the transferring hydrogen atom by deuterium should give a major change in the value of the free energy of activation, and, hence, a large kinetic isotope effect,[26] as indeed observed experimentally and reported above in Figure 2. Moreover, the transition states are late with long C–H and short O–H distances for ^{5}**TS**$_{HAT1}$ (1.448 and 1.163 Å, respectively), while the transferring hydrogen atom in ^{5}**TS**$_{HAT2}$ is closer to the donor hydroperoxo group (1.106 Å) than the accepting alcohol oxygen atom (1.327 Å).

In the enol-form, a nucleophilic attack takes place of the manganese(III)-peroxo group on the double bond through a C–O bond formation via ^{5}**TS1**. This transition state has a relatively large imaginary frequency of i735 cm^{-1} due to the simultaneous C–O bond formation and proton transfer from enol to peroxo. Thus, the peroxo bond weakens to 1.427 Å and a C–O interaction of 1.995 Å is formed.

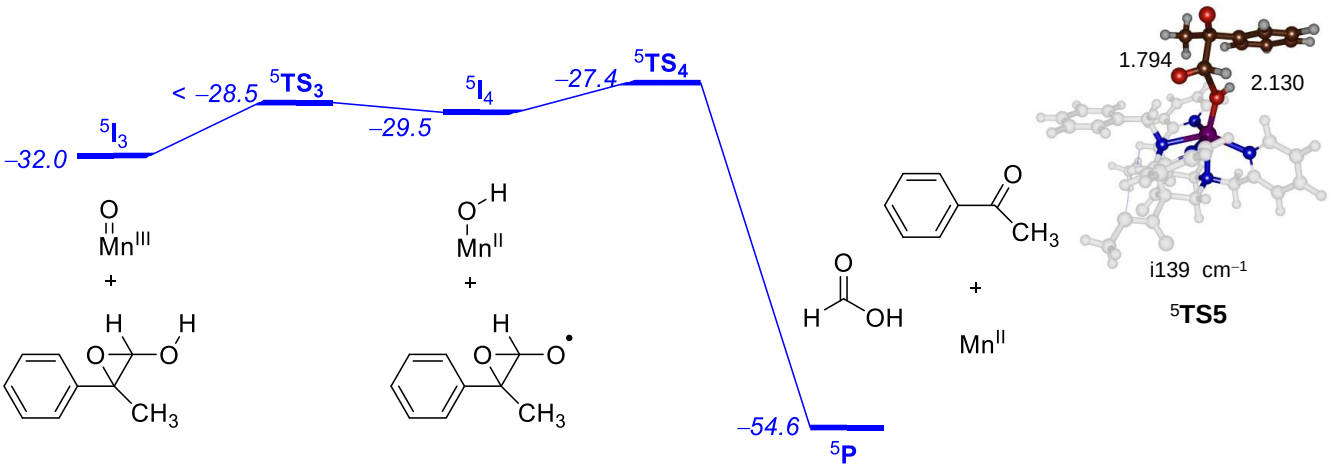

Figure 4. Potential energy profile (UB3LYP/BS2//UB3LYP/BS1+ZPE) for oxygen atom transfer from ^{5}I$_3$ leading to products with energies in kcal mol^{-1}. Transition state structure gives distances in angstroms and the imaginary frequency in cm^{-1}.

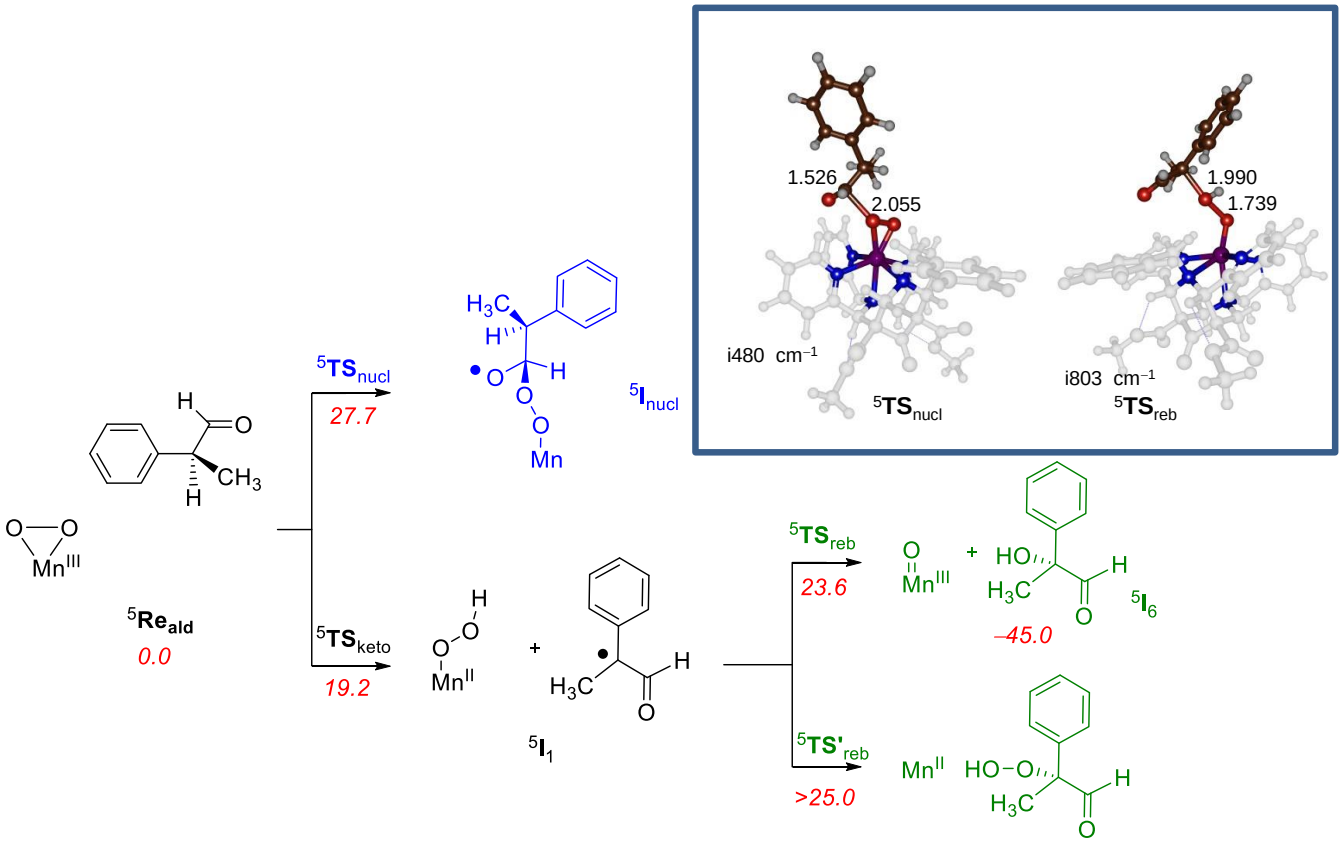

Figure 5. Alternative nucleophilic transition states along the pathway of aldehyde deformylation by side-on manganese(III)-peroxo as calculated at UB3LYP/BS2//UB3LYP/BS1+ZPE level of theory. Energies are in kcal mol^{-1}. Transition state structures give distances in angstroms and the imaginary frequency in cm^{-1}.

After the transition state the system relaxes to a local minimum that has a single bond for the C–O interaction and a radical on the neighboring carbon atom. In addition, the dioxygen moiety moves from a side-on to an end-on conformation. The dioxygen bond cleaves in ^{5}**TS2** at an energetic cost of 19.8 kcal mol^{-1}. In this step simultaneous to the O–O bond breaking an epoxide ring is formed to give a low-energy manganese(III)-oxo species. The imaginary mode in the transition state indeed reflects the O–O bond cleavage on the one hand and the epoxide ring-closure on the other hand.

The next stage in the mechanism from epoxide to final deformylation products is given in Figure 4. Thus, the manganese(III)-oxo group abstracts a hydrogen atom in ^{5}I$_3$

from the alcohol position of substrate, which breaks the epoxide ring to form a complex between manganese(II)-hydroxo and a radical (^{5}**I**$_4$). This step has an almost barrierless reaction pathway via ^{5}**TS3** and hence the ^{5}**TS3** structure could not be properly characterized. An estimate from the geometry scan predicts it to be less than 1 kcal mol^{-1} in energy above the value of ^{5}**I**$_4$. The subsequent OH rebound leads to simultaneous epoxide ring-opening, C–C bond cleavage and the formation of formic acid and methylphenylketone products via transition state ^{5}**TS4**. The imaginary frequency of i139 cm^{-1} indeed reflects the C–C bond breaking and the dissociation of methylphenylketone from the complex. At the same time the OH rebound to the HCO leaving group gives formic acid as the second product. The overall reaction mechanism has two highly exothermic reaction steps, namely the formation of the manganese(III)-oxo species (^{5}**I**$_3$) and the final reaction step leading to methylphenylketone and formic acid products. These two steps will be irreversible, although other reactions steps may be reversible.

In summary, the lowest energy pathway for aldehyde deformylation by side-on manganese(III)-peroxide of 2-PPA is α-hydrogen atom abstraction followed by reshuttle and tautomerization to form the enol form and nucleophilic attack on the olefin bond. Oxygen atom transfer then gives epoxide that through a low-barrier hydrogen atom transfer gives formic acid and methylphenylketone products.

Alternative mechanisms. Several alternative pathways for aldehyde deformylation by side-on manganese(III)-peroxo complexes were considered, as shown in Figure 5. Firstly, a direct nucleophilic attack on the carbonyl group of 2-PPA was considered by side-on manganese(III)-peroxo. The nucleophilic pathway proceeds via a transition state ^{5}**TS**$_{nucl}$ to form the nucleophilic addition intermediate ^{5}**I**$_{nucl}$ (Figure 5). Similarly to the results reported previously,[9] this is a high-energy pathway with a barrier of $\Delta E^{\ddagger}$+ZPE = 27.7 kcal mol^{-1}. The transition state has an imaginary frequency of i480 cm^{-1}, which reflects the C–O bond formation between peroxo and carbonyl moieties and simultaneously the peroxo moves from side-on to end-on. Clearly, the direct nucleophilic addition from side-on peroxo is well higher in energy than the hydrogen atom abstraction reported above in Figure 4 by at least 8.5 kcal mol^{-1} and hence will not be competitive.

We also investigated mechanisms starting from the manganese(III)-hydroperoxo intermediate ^{5}**I**$_1$ and, in particular, looked at OH rebound to form manganese(III)-oxo and 2-hydroxo-2-phenyl-propionaldehyde (^{5}**I**$_6$). Although, ^{5}**I**$_6$ is considerably more stable than the epoxide intermediate ^{5}**I**$_3$ reported above. Actually, its formation barrier is considerably higher in energy. Therefore, despite the fact that ^{5}**I**$_6$ is a more stable intermediate than ^{5}**I**$_3$ the preferred reaction intermediate leading to aldehyde deformylation will pass ^{5}**I**$_3$. The OH rebound transition state (^{5}**TS**$_{reb}$) has typical features seen before for OH transfer from iron(III)-hydroperoxo complexes,[27] with simultaneous O–O cleavage and C–O bond formation in a concerted reaction step. The OH group is located midway between donor and acceptor groups through long interactions of 1.990 and 1.739 Å.

Additionally, various other pathways were tested (see Supporting Information) including rebound of the OH group to the aldehyde carbon atom. However, this OH rebound pathway formed a biradical species that is very high in energy (>50 kcal mol^{-1}). Also, OOH transfer from the manganese(II)-hydroperoxo intermediate (^{5}**I**$_1$) to the radical gave a barrier (^{5}**TS'**$_{reb}$) of well over 25 kcal mol^{-1} in energy. Unfortunately, no subsequent pathways leading to aldehyde deformylation products could be identified, and therefore the mechanism was ruled out.

Finally, a mechanism was considered for nucleophilic attack of manganese(III)-peroxo on the secondary carbon atom of the enol form of 2-PPA. The intermediate formed through this pathway is high in energy (>40 kcal mol^{-1} with respect to ^{5}**Re**$_{ald}$) and consequently the pathway is ruled out as a viable reaction mechanism.

In conclusion, the lowest energy reaction mechanism for aldehyde deformylation by manganese(III)-peroxo complexes we have identified starts with hydrogen atom abstraction from the α-position followed by a reshuttle, whereby the aldehyde is converted into an enol that can efficiently react via nucleophilic addition with the side-on manganese(III)-peroxo.

Discussion.

To understand the unusual mechanism found for aldehyde deformylation by manganese(III)-peroxo complexes, we analyzed the structure and electronic configuration of all species in detail and set up valence bond and thermochemical cycles to explain the mechanism and rationalize the observed reactivities.

Thermochemical modelling. Let us first try to predict the hydrogen atom abstraction barriers for the keto and enol form of 2-PPA by side-on manganese(III)-peroxo complexes. The driving force for the hydrogen atom abstraction, can be written as the difference in energy between the C–H/O–H bond that is broken and the O–H bond formed of the manganese(II)-hydroperoxo, which in general terms using substrate SubH is given in Eq 4.

$$[Mn^{III}(O_2)(L^2)]^+ + SubH \rightarrow [Mn^{II}OOH(L^2)]^+ + Sub^{\bullet} \quad (4)$$

The overall reaction (Eq 4) has an energy corresponding to the driving force ΔE_{rp} and can be written as the difference between two bond dissociation free energies (BDFEs) of the bonds that are formed and broken as defined in Eq 5 – 7. Thus, the BDFE values for the substrate C–H bond of the aldehyde from of 2-PPA and the O–H bond of the enol form of 2-PPA are defined as through Eq 5 as BDFE$_{CH}$(2-PPA) and BDFE$_{OH}$(2-PPA). Values were calculated from a full geometry optimization of 2-PPA and 2-PPA with the transferring hydrogen atom removed (Sub$^{\bullet}$) and the free

energy difference obtained from Eq 5. Subsequently, we calculated the $BDFE_{OH}$ value of the manganese(II)-hydroperoxo species from its free energy difference with the manganese(III)-peroxo and a hydrogen atom (Eq 6) as defined as $BDFE_{OH}$(Ox).

$$SubH \rightarrow Sub^{\bullet} + H^{\bullet} + BDFE_{AH} \quad (5)$$

$$[Mn^{II}OOH(L^2)]^+ \rightarrow [Mn^{III}(O_2)(L^2)]^+ + H^{\bullet} + BDFE_{OH} \quad (6)$$

$$\Delta G_{rp} = BDFE_{AH}(SubH) - BDFE_{OH}(Ox) \quad (7)$$

Therefore, the driving force for the hydrogen atom abstraction from substrate (ΔG_{rp}), be it in the keto or enol form, by $[Mn^{III}(O_2)(L^2)]^+$ can be written in terms of BDFE of donor and acceptor groups, Eq 7. We calculate BDFE values of 66.1 and 55.9 kcal mol^{-1} for hydrogen atom abstraction from the keto and enol form of 2-PPA, respective-ly. In agreement with the potential energy landscape in Figure 4 above, these $BDFE_{CH}$ values implicate that it is easier to abstract a hydrogen atom from the enol-form of substrate than from the α-position of the aldehyde.

Furthermore, $BDFE_{OH}$ values of 56.6 and 61.1 kcal mol^{-1} were obtained for $[Mn^{II}OOH(L^1)]^+$ and $[Mn^{II}OOH(L^2)]^+$, respectively. Consequently, the driving forces for hydro-gen atom abstraction of $[Mn^{III}(O_2)(L^2)]^+$ from 2-PPA in its keto form is ΔG = 5.0 kcal mol^{-1}, which is in excellent agreement with the reaction free energy from $^5\mathbf{Re}_{ald}$ to $^5\mathbf{I}_1$ of 6.2 kcal mol^{-1} (Table S3, Supporting Information). Similarly, the driving force from hydrogen atom abstraction of the enol form of 2-PPA by $[Mn^{III}(O_2)(L^2)]^+$ of ΔG = –5.2 kcal mol^{-1} matches the free energy difference between $^5\mathbf{Re}_{enol}$ and $^5\mathbf{I}_1$ reasonably well.

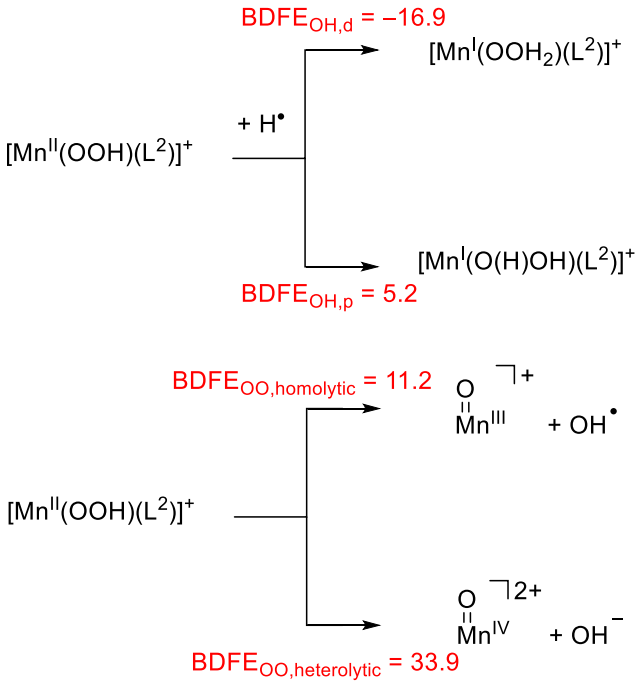

Scheme 3. Reactivity channels of $[Mn^{II}(OOH)(L^2)]^+$ through hydrogen atom abstraction (top) or O–O bond cleavage (bottom).

To compare the $BDFE_{CH}$ of 2-PPA with typical substrates used in hydrogen atom transfer reactions, we calculated the $BDFE_{CH}$ of 1,4-cyclohexadiene. Interestingly, the $BDFE_{CH}$ of 1,4-cyclohexadiene is 61.9 kcal mol^{-1}, which is midway in between the values for breaking the C–H bond of the keto-form of 2-PPA and the O–H bond of the enol form. Therefore, theory would expect the first aliphatic hydrogen atom abstraction of 1,4-cyclohexadiene by side-on manganese(III)-peroxo to proceed with similar rate constants as 2-PPA. However, no benzene products are obtained, which probably means that the subsequent reaction step between manganese(II)-hydroperoxo and the C_6H_7 radical does not lead to products and a further hydrogen atom abstraction is hampered. As side-on manganese(III)-peroxo can abstract a hydrogen atom from 2-PPA this implies that the cyclohexadiene reaction is prevented due to an energetically unfavorable second hydrogen atom abstraction performed by the manganese(II)-hydroperoxo species. Thus, side-on manganese(III)-peroxo will not react with aliphatic C–H bonds through substrate hydroxylation.

To test this hypothesis, we calculated the hydrogen atom abstraction energy by $[Mn^{II}OOH(L^2)]^+$ at either the distal or proximal oxygen atom, Scheme 3. In particular, we calculated the diabatic hydrogen atom abstraction energy by the manganese(II)-hydroperoxo species as a full geometry optimization of either $[Mn^{I}(OOH_2)(L^2)]^+$ or $[Mn^{I}(O(H)OH)(L^2)]^+$ led to dissociation of both complexes. Proximal donation of a hydrogen atom has a driving force of only 5.2 kcal mol^{-1}, whereas proximal donation gives an endothermic BDFE value. Consequently, despite the fact that manganese(III)-peroxo is able to abstract hydrogen atoms from weak aliphatic C–H bonds, the resulting manganese(II)-hydroperoxo is inactive and thermodynamically unable to react further to give either alcohols or a dehydrogenation of substrate.

To find out, whether the manganese(II)-hydroperoxo has other catalytic abilities, we calculated its homolytic and heterolytic O–O bond cleavage free energies, see bottom part of Scheme 3. Similar to that seen for nonheme iron(III)-hydroperoxo complexes,[28] also here the heterolytic cleav-age is high in free energy (>30 kcal mol^{-1}) and can be ruled out. Homolytic cleavage is endothermic by 11.2 kcal mol^{-1} and, therefore, although a slow process, may be feasible. As such, the only probably reaction pathway for manganese(II)-hydroperoxo is homolytic cleavage of the O–O bond but will only be possible if the bond that is subsequently formed is strong enough to balance the energetic cost of the O–O bond breaking mechanism.

Valence bond rationalization of the mechanism. Figure 6 gives the electronic delineation of the properties a rate determining reaction barrier should possess and how this links to the properties of reactants and products.[9,21,29] Thus, as an example we consider the hydrogen atom abstraction reaction from a reactant complex (**Re**) via a tran-

sition state ($\mathbf{TS}_{HAT}$) leading to a radical intermediate ($\mathbf{I}_{HAT}$). We now envisage the local minima to reside in a parabolic function (y, representing the potential energy) along the reaction coordinate axis (x) for the hydrogen atom abstraction with the reactants in the origin (x = 0) and the radical intermediate at the value x = 1. Mathematically, the potential energy functions for the reactant and intermediate states can then be described as shown in Eq 8 and 9 with a, b, c, and d some constants that determine the shape and curvature of the two parabolic functions.

$$y_{Re} = ax^2 \quad (8)$$

$$y_I = bx^2 + cx + d \quad (9)$$

It has been shown through valence bond modelling that the transition state connecting two local minima is located nearby the curve crossing of the VB curves of the reactant and product wave functions.[30] If we assume the crossing happens in x = ½ then we can derive a function for the crossing point of the two curves as a function of two variables, namely the difference in energy between the two functions in x = 0, i.e. the Franck-Condon energy in the reactants ($E_{FC,Re}$), and the driving force for the hydrogen atom abstraction reaction (ΔE_{rp}), Eq 10.

$$\Delta E_{cross} = ¼\ E_{FC,Re} + ¾\ \Delta E_{rp} \quad (10)$$

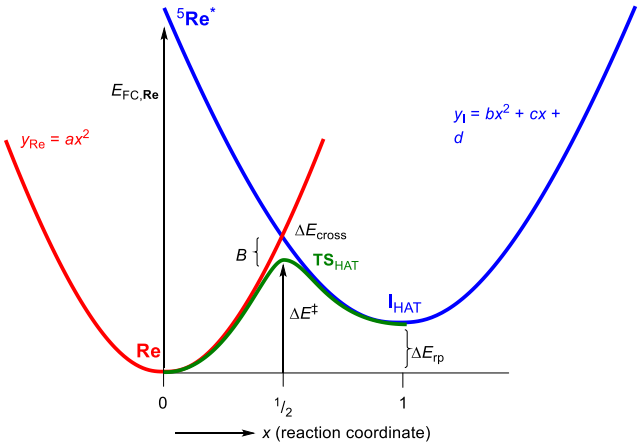

Figure 6. Definition of a reaction barrier and its connection to the vertical excitation energy in the reactants ($E_{FC,R}$) and the driving force for the reaction (ΔE_{rp}).

Further, it has been shown that the curve crossing energy is a fraction B (the resonance energy) above the actual transition state,[30] so that the height of the reaction barrier can be estimated from the Franck-Condon energy between the two states in the reactants, the driving force and the resonance energy. Previously, we used this procedure successfully to predict trends in aromatic hydroxylation reactions by iron(IV)-oxo porphyrin cation radical models and benchmarked the results against experimental rate constants.[31] In addition, we predicted regioselectivity ratios of aliphatic hydroxylation versus decarboxylation reactions in cytochrome P450 peroxygenase enzymes using VB models.[32]

Subsequently, we attempted to estimate the Franck-Condon energies ($E_{FC,Re}$) from electronic changes along the reaction mechanism for hydrogen atom abstraction (HAT) and nucleophilic addition (NA). Figure 7 displays the electronic changes during the hydrogen atom abstraction step between $^5[Mn^{III}(O_2)(L^2)]^+$ and substrate. Obviously, the hydrogen atom abstraction implies the breaking of a substrate C–H (or O–H in the case of the enol structure) bond orbital of the substrate (σ_{CH}) that splits into two atomic orbitals ($2p_C$ and $1s_H$ each with one electron). Therefore, the value of $E_{FC,Re}$ will contain the energy to break the σ_{CH} bond, $E_{\sigma(C-H)}$.

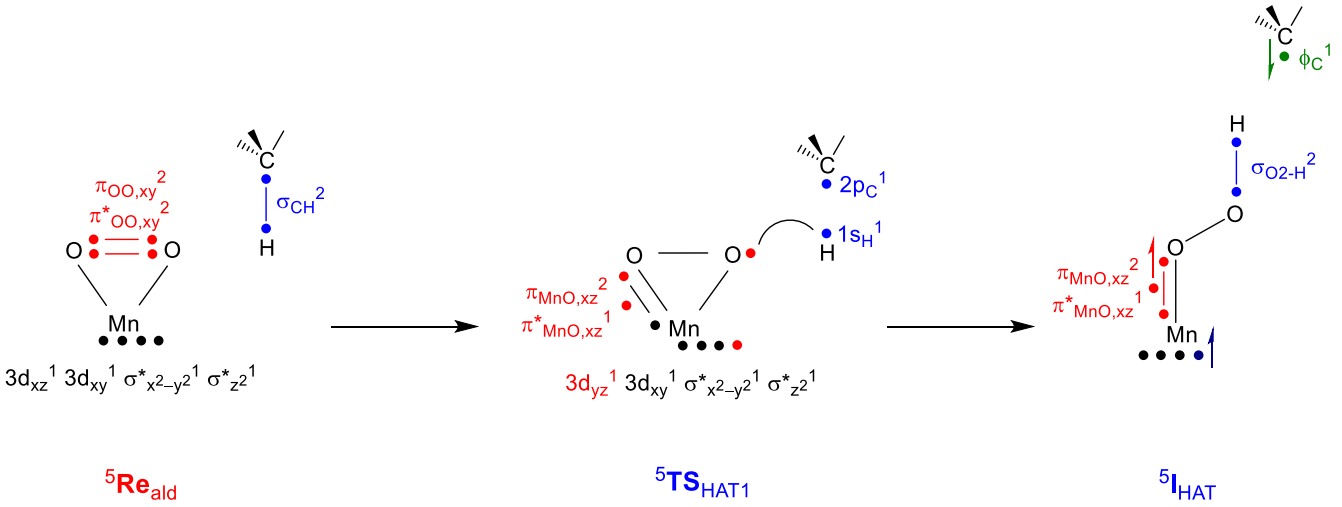

Figure 7. Electronic changes during the hydrogen atom abstraction from substrate by quintet spin side-on manganese(III)-peroxo. Dots represent electrons and lines between dots a bond orbital.

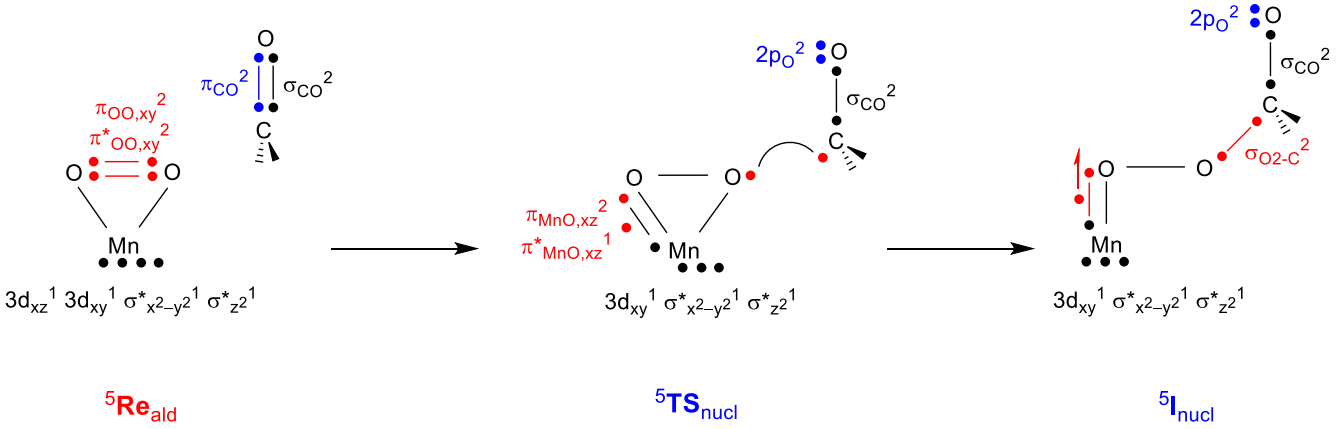

Figure 8. Electronic changes during the nucleophilic addition from substrate by quintet spin side-on manganese(III)-peroxo. Dots represent electrons and lines between dots a bond orbital.

In addition, the peroxo double bond ($\pi_{00,xy}/\pi^*_{00,xy}$) breaks with energy $E_{\pi/\pi^*00,xy}$ and the four electrons are re-distributed over the manganese-peroxo system: Two of those will pair up with the $3d_{xz}$ on manganese to form a three-electron MnO bond ($\pi_{MnO,xz}^2\ \pi^*_{MnO,xz}{}^1$), the third electron stays as a 2p on oxygen and will pair up with $1s_H$ to form the O–H orbital (σ_{O2-H}), while the fourth electron is promoted into the virtual $3d_{yz}$ orbital on manganese ($E_{exc,Mn}$). Consequently, the Franck-Condon energy should correlate with the breaking of the $\pi_{MnO,xz}$ orbitals, the formation of the O–H orbital, the breaking of the C–H orbital and the electron transfer from peroxo to manganese, Eq 11.

$$E_{FC,Re,HAT} = E_{\sigma(C-H)} + E_{\pi/\pi^*00,xy} + E_{exc,Mn} \qquad (11)$$

The $E_{\sigma(C-H)}$ was determined from the adiabatic values using Eq 5 above as 82.6 kcal mol^{-1}. The $E_{\pi/\pi^*00,xy}$ energy was determined from the orbital energy difference of the α-type $\pi_{00,xy}$ and $\pi^*_{00,xy}$ orbitals in the quintet spin reactant complex (78.2 kcal mol^{-1}), whereas $E_{exc,Mn}$ was taken as the energy difference between the $\pi^*_{00,xy}$ and π^*_{yz} orbitals with β-spin. These values gave us a prediction of $E_{FC,Re,HAT}$, whereas the energy difference of the BDE_{CH} of the substrate and the BDE_{OH} of $^6[MnOOH(L^2)]^+$ gave ΔE_{rp} = 8.0 kcal mol^{-1}. Based on Eq 10 and 11 we estimated the hydrogen atom abstraction barrier from the keto position as $\Delta E^{\ddagger}_{VB,HAT}$ = 18.5 kcal mol^{-1}. For comparison, using transition state theory, the experimental second-order rate constant of k_2 = 0.142 M^{-1} s^{-1} corresponds to a free energy of activation of $\Delta G^{\ddagger}_{2,exp}$ = 18.9 kcal mol^{-1} at 15°C. Therefore, our DFT model predicts the hydrogen atom abstraction barrier perfectly and explains the contributions from orbital/bond breaking and forming processes.

Finally, we analyze the VB electronic configuration changes for the nucleophilic reaction of manganese(III)-peroxo with aldehyde in Figure 8. Similarly to the hydrogen atom abstraction step, the $\pi_{00,xy}/\pi^*_{00,xy}$ orbital couple is rehybridized and converted back into atomic orbitals, whereby again two of those electrons will form a new three-electron bond along the Mn–O axis ($\pi_{MnO,xz}^2\ \pi^*_{MnO,xz}{}^1$).

The remaining two electrons originating from the $\pi_{00,xy}/\pi^*_{00,xy}$ orbitals are donated into the new σ-bond for the C–O interaction. This results in the breaking of the π-bond of the carbonyl (in the keto-form) or olefin (in the enol-form) bond of the substrate.

To estimate the VB barrier for the nucleophilic attack, we again took the energy to break the $\pi_{00,xy}/\pi^*_{00,xy}$ orbitals ($E_{\pi/\pi^*oo,xy}$) as well as the energy to break the double bond ($E_{\pi,Sub}$), Eq 12. The energy $E_{\pi,Sub}$ for the keto and enol forms of the substrate was determined from the singlet-triplet energy gap in the isolated forms as 83.1 and 77.5 kcal mol^{-1}, respectively. That way, we predict a nucleophilic barrier height of 24.8 kcal mol^{-1} for direct attack of aldehyde on side-on manganese(III)-peroxo. This value is in good quantitative agreement with the DFT barrier reported above and explains the electrostatic interactions relevant for the barrier height. It also shows that it will be easier for the enol form to react through nucleophilic addition then the keto form as the singlet-triplet energy gap in the double bond is much higher.

$$E_{FC,Re,NA} = E_{\pi,Sub} + E_{\pi/\pi^*OO,xy} \quad (12)$$

Conclusions.

In this work a combined experimental and computational study is reported on aldehyde deformylation by side-on manganese(III)-peroxo complexes. We identify a novel reaction mechanism that starts with a hydrogen atom abstraction and reshuttle to give a keto-enol tautomerization in the substrate as rate determining step. Subsequently, a nucleophilic attack on the olefin bond in the enol form lead to a low-energy mechanism to products. Alternative pathways were tested and ruled out. A detailed thermochemical and valence bond analysis of the structures and of intermediates and reactants explains the origin of the keto-enol tautomerization. Thus, in the enol form the olefin π-bond is easy to break, whereas breaking the carbonyl π-bond is more energetically demanding. As the reaction starts with a hydrogen atom abstraction from aldehyde, we also considered the manganese(III)-peroxo species as a general oxidant for substrate hydroxylation and desaturation reactions. Unfortunately, high reaction barriers for radical rebound are encountered and substrate hydroxylation and desaturation are unfeasible pathways at room temperature.

ASSOCIATED CONTENT

Supporting Information. Tables with energies, group spin densities and charges as well as Cartesian coordinates of all structures reported is provided as Supporting Information. This material is available free of charge via the Internet at http://pubs.acs.org.

AUTHOR INFORMATION

Corresponding Author

* sam.devisser@manchester.ac.uk (SPdV); sastricv@iitg.ernet.in (CVS).

Author Contributions

The manuscript was written through contributions of all authors. All authors have given approval to the final version of the manuscript.

ACKNOWLEDGMENT

FGCR thanks the Conacyt (Mexico) for a studentship. DK & SPdV thank the University of Manchester for a Targeting GCRF Applications in Industrial Biotechnology: Enhancing International Collaborations award. Research support was provided by the Department of Science and Technology (SERB), India (EMR/2014/000279) to CVS. DK and JK acknowledge financial support from DBT, New Delhi (BT/PR14510/BID/07/334/2010).

ABBREVIATIONS

SOD, superoxide dismutase; PSII, Photosystem II; DFT, density functional theory; KIE, kinetic isotope effect; PPA, phenylpropionaldehyde; TEA, triethylamine; ESI-MS, electrospray ionization – mass spectrometry; PCM, polarized continuum model; VB, valence bond; CHD, cyclohexadiene.

REFERENCES

1. See, e.g., (a) Solomon, E. I.; Brunold, T. C.; Davis, M. I.; Kemsley, J. N.; Lee, S.-K.; Lehnert, N.; Neese, F.; Skulan, A. J.; Yang, Y.-S.; Zhou, J. *Chem. Rev*. **2000**, *100*, 235–349. (b) Bugg, T. D. H. *Curr. Opin. Chem. Biol*. **2001**, *5*, 550–555. (c) Ryle, M. J.; Hausinger, R. P. *Curr. Opin. Chem. Biol*. **2002**, *6*, 193–201. (d) Costas, M.; Mehn, M. P.; Jensen, M. P.; Que Jr, L. *Chem. Rev*. **2004**, *104*, 939–986. (e) Abu-Omar, M. M.; Loaiza, A.; Hontzeas, N. *Chem. Rev*. **2005**, *105*, 2227–2252. (f) Krebs, C.; Fujimori, D. G.; Walsh, C. T.; Bollinger Jr, J. M. *Acc. Chem. Res*. **2007**, *40*, 484–492. (g) Bruijnincx, P. C. A.; van Koten, G.; Klein Gebbink, R. J. M. *Chem. Soc. Rev*. **2008**, *37*, 2716–2744. (h) Solomon, E. I.; Light, K. M.; Liu, L. V.; Srnec, M.; Wong, S. D. *Acc. Chem. Res*. **2013**, *46*, 2725–2739. (i) McDonald, A. R.; Que Jr, L. *Coord. Chem. Rev*. **2013**, *257*, 414–428.

2. (a) Zhu, W.; Richards, N. G. J. *Essays Biochem*. **2017**, *61*, 259–270. (b) Aguirre, J. D.; Culotta, V. C. *J. Biol. Chem*. **2012**, *287*, 13541–13548.

3. (a) Jackson, T. A.; Brunold, T. C. *Acc. Chem. Res*. **2004**, *37*, 461–470. (b) Streit, B. R.; Blanc, B.; Lukat-Rodgers, G. S.; Lukat-Rodgers, K. R.; Dubois, J. L. *J. Am. Chem. Soc*. **2010**, *132*, 5711–5724. (c) Hofbauer, S.; Gruber, C.; Pirker, K. F.; Sündermann, A.; Schaffner, I.; Jakopitsch, C.; Oostenbrink, C.; Furtmüller, P. G.; Obinger, C. *Biochemistry* **2014**, *53*, 3145–3157. (d) Grove, L. E.; Xie, J.; Yikilmaz, E.; Miller, A.-F.; Brunold, T. C. *Inorg. Chem*. **2008**, *47*, 3978–3992. (e) Kenkel, I.; Franke, A.; Dürr, M.; Zahl, A.; Dücker-Benfer, C.; Langer, J.; Filipović, M. R.; Yu, M.; Puchta, R.; Fiedler, S. R.; Shores, M. P.; Goldsmith, C. R.; Ivanović-Burmazović, I. *J. Am. Chem. Soc*. **2017**, *139*, 1472–1484. (f) Miller, A.-F. *FEBS. Lett*. **2012**, *586*, 585–595. (g) Lee, A. Q.; Streit, B. R.; Zdilla, M. J.; Abu-Omar, M. M.; DuBois, J. L. *Proc. Natl. Acad. Sci. USA* **2008**, *105*, 15654–15659.

4. (a) Vinyard, D. J.; Ananyev, G. M.; Dismukes, G. C. *Annu. Rev. Biochem*. **2013**, *82*, 577–606. (b) Renger, G.; Renger, T. *Photosynth. Res*. **2008**, *98*, 53–80. (c) Barber, J. *Quart. Rev. Biophys*. **2003**, *36*, 71–89. (d) Siegbahn, P. E. M. *Chem. Eur. J*. **2008**, *14*, 8290–8302.

5. (a) Kryatov, S. V.; Rybak-Akimova, E. V.; Schindler, S. *Chem. Rev*. **2005**, *105*, 2175–2226. (b) Nam, W. *Acc. Chem. Res*. **2007**, *40*, 522–531. (c) Sahu, S.; Goldberg, D. P. *J. Am. Chem. Soc*. **2016**, *138*, 11410–11428. (d) Saisaha, P.; de Boer, J. W.; Browne, W. R. *Chem. Soc. Rev*. **2013**, *42*, 2059–2074.

6. (a) Roelfes, G.; Vrajmasu, V.; Chen, K.; Ho, R. Y. N.; Rohde, J.-U.; Zondervan, C.; la Crois, R. M.; Schudde, E. P.; Lutz, M.; Spek, A. L.; Hage, R.; Feringa, B. L.; Münck, E.; Que Jr, L. *Inorg. Chem*. **2003**, *42*, 2639–2653. (b) Annaraj, J.; Suh, Y.; Seo, M. S.; Kim, S. O.; Nam, W. *Chem. Commun*. **2005**, 4529–4531. (c) Thibon, A.; Bartoli, J.-F.; Bourcier, S.; Banse, F. *Dalton Trans*. **2009**, 9587–9584. (d) Mukherjee, A.; Cranswick, M. A.; Chakrabarti, M.; Paine, T. K.; Fujisawa, K.; Münck, E.; Que Jr, L. *Inorg. Chem*. **2010**, *49*, 3618–3628. (e) Cho, J.; Jeon, S.; Wilson, S. A; Liu, L. V.; Kang, E. A.; Braymer, J. J.; Lim, M. H.; Hedman, B.; Hodgson, K. O.; Valentine, J. S.; Solomon, E. I.; Nam, W. *Nature* **2011**, *478*, 502–505.

7. (a) Annaraj, J.; Cho, J.; Lee, Y.-M.; Kim, S. Y.; Latifi, R.; de Visser, S. P.; Nam, W. *Angew. Chem. Int. Ed*. **2009**, *48*, 4150–4153. (b) Leto, D. F.; Chattopadhyaay, S.; Day, V. W.; Jackson, T. A. *Dalton Trans*. **2013**, *42*, 13014–13025. (c) Zlatar, M.; Gruden, M.; Vassilyeva, O. Y.; Buvaylo, E. A.; Ponomarev, A. N.; Zvyagin, S. A.; Wosnitza, J.; Krzystek, J.; Garcia-Fernandez, P.; Duboc, C. *Inorg. Chem*. **2016**, *55*, 1192–1201. (d) Lee, C.-M.; Chuo, C.-H.; Chen, C.-H.; Hu, C.-C.; Chiang, M.-H.; Tseng, Y.-J.; Hu, C.-H.; Lee, G.-H. *Angew. Chem. Int. Ed*. **2012**, *51*, 5427–5430. (e) Gennari, M.; Brazzolotto, D.; Pécaut, J.; Cherrier, M. V.; Pollock, C. J.; DeBeer, S.; Retegan, M.; Pantazis, D. A.; Neese, F.; Duboc, C. *J. Am. Chem. Soc*. **2015**, *137*, 8644–8653. (f) Brazzolotto, D.; Cantú Reinhard, F. G.; Smith-Jones, J.; Retegan, M.; Amidani, L.; Faponle, A. S.; Ray, K.; Philouze, C.; de Visser, S. P.; Gennari, M.; Duboc, C. *Angew. Chem. Int. Ed*. **2017**, *56*, 8211–8215.

8. (a) Coggins, M. K.; Kovacs, J. A. *J. Am. Chem. Soc*. **2011**, *133*, 12470–12473. (b) Coggins, M. K.; Martin-Diaconescu, V.; DeBeer, S.; Kovacs, J. A. *J. Am. Chem. Soc*. **2013**, *135*, 4260–4272. (c) Colmer, H. E.; Howcroft, A. W.; Jackson, T. A. *Inorg. Chem*. **2016**, *55*, 2055–2069. (d) Cho, J.; Sarangi, R.; Nam, W. *Acc. Chem. Res*. **2012**, *45*, 1321–1330. (e) Zhang, Q.; Bell-Taylor, A.; Bronston, F. M.; Gorden, J. D.; Goldsmith, C. R. *Inorg. Chem*. **2017**, *56*, 773–782.

9. Barman, P.; Upadhyay, P.; Faponle, A. S.; Kumar, J.; Nag, S. S.; Kumar, D.; Sastri, C. V.; de Visser, S. P. *Angew. Chem. Int. Ed*. **2016**, *55*, 11091–11095.

10. (a) Vardhaman, A. K.; Barman, P.; Kumar, S.; Sastri, C. V.; Kumar, D.; de Visser, S. P. *Angew. Chem. Int. Ed*. **2013**, *52*, 12288–12292. (b) Kumar, S.; Faponle, A. S.; Barman, P.; Vardhaman, A. K.; Sastri, C. V.; Kumar, D.; de Visser, S. P. *J. Am. Chem. Soc.* **2014**, *136*, 17102–17115. (c) Barman, P.; Faponle, A. S.; Vardhaman, A. K.; Angelone, D.; Löhr, A.-M.; Browne, W. R.; Comba, P.; Sastri, C. V.; de Visser, S. P. *Inorg. Chem*. **2016**, *55*, 10170–10181.

11. Armarego, W. L. F. In *Purification of Laboratory Chemicals*, Perrin, D. D. (Ed.), Pergamon Press, Oxford, **1997**.

12. (a) Börzel, H.; Comba, P.; Hagen, K. S.; Lampeka, Y. D.; Lienke, A.; Linti, G.; Merz, M.; Pritzkow, H.; Tsymbal, L. V. *Inorg. Chim. Acta*. **2002**, *337*, 407–419. (b) Comba, P.; Kuwata, S.; Linti, G.; Pritzkow, H.; Tarnai, M.; Wadepohl, H. *Chem. Commun*. **2006**, 2074–2076. (c) Comba, P.; Kanellakopulos, B.; Katsichtis, C.; Lienke, A.; Pritzkow, H.; Rominger, F. *J. Chem. Soc. Dalton Trans*. **1998**, 3997–4001. (d) Barman, P.; Vardhaman, A. K.; Martin, B.; Wörner, S. J.; Sastri, C. V.; Comba, P. *Angew. Chem. Int. Ed.* **2015**, *54*, 2095–2099.

13. Goto, Y.; Wada, S.; Morishima, I.; Watanabe, Y. *J. In-org. Biochem*. **1998**, *69*, 241–247.

14. (a) de Visser, S. P.; Quesne, M. G.; Martin, B.; Comba, P.; Ryde, U. *Chem. Commun*. **2014**, *50*, 262–282. (b) Sainna, M. A.; Kumar, S.; Kumar, D.; Fornarini, S.; Crestoni, M. E.; de Visser, S. P. *Chem. Sci*. **2015**, *6*, 1516–1529.

15. *Gaussian* 09, Revision C.01, Frisch, M. J.; Trucks, G. W.; Schlegel, H. B.; Scuseria, G. E.; Robb, M. A.; Cheeseman, J. R.; Scalmani, G.; Barone, V.; Mennucci, B.; Petersson, G. A.; Nakatsuji, H.; Caricato, M.; Li, X.; Hratchian, H. P.; Izmaylov, A. F.; Bloino, J.; Zheng, G.; Sonnenberg, J. L.; Hada, M.; Ehara, M.; Toyota, K.; Fukuda, R.; Hasegawa, J.; Ishida, M.; Nakajima, T.; Honda, Y.; Kitao, O.; Nakai, H.; Vreven, T.; Montgomery Jr, J. A.; Peralta, J. E.; Ogliaro, F.; Bearpark, M.; Heyd, J. J.; Brothers, E.; Kudin, K. N.; Staroverov, V. N.; Keith, T.; Kobayashi, R.; Normand, J.; Raghavachari, K.; Rendell, A.; Burant, J. C.; Iyengar, S. S.; Tomasi, J.; Cossi, M.; Re-ga, N.; Millam, J. M.; Klene, M.; Knox, J. E.; Cross, J. B.; Bakken, V.; Adamo, C.; Jaramillo, J.; Gomperts, R.; Stratmann, R. E.; Yazyev, O.; Austin, A. J.; Cammi, R.; Pomelli, C.; Ochterski, J. W.; Martin, R. L.; Morokuma, K.; Zakrzewski, V. G.; Voth, G. A.; Salvador, P.; Dannenberg, J. J.; Dapprich, S.; Daniels, A. D.; Farkas, O.; For-esman, J. B.; Ortiz, J. V.; Cioslowski, J.; Fox, D. J. Gaussian, Inc., Wallingford CT, **2010**.

16. Tomasi, J.; Mennucci, B.; Cammi, R. *Chem. Rev*. **2005**, *105*, 2999–3093.

17. (a) Becke, A. D. *J. Chem. Phys*. **1993**, *98*, 5648–5652. (b) Lee, C.; Yang, W.; Parr, R. G. *Phys. Rev. B* **1988**, *37*, 785–789.

18. (a) Hay, P. J.; Wadt, W. R. *J. Chem. Phys*. **1985**, *82*, 270–283. (b) Hehre, W. J.; Ditchfield R.; Pople, J. A. *J. Chem. Phys*. **1972**, *56*, 2257–2262.

19. (a) de Visser, S. P. *J. Am. Chem. Soc*. **2010**, *132*, 1087–1097. (b) Quesne, M. G.; Senthilnathan, D.; Singh, D.; Kumar, D.; Maldivi, P.; Sorokin, A. B.; de Visser, S. P. *ACS Catal*. **2016**, *6*, 2230–2243.

20. (a) Cantú Reinhard, F. G.; Faponle, A. S.; de Visser, S. P. *J. Phys. Chem. A* **2016**, *120*, 9805–9814. (b) Yang, T.; Quesne, M. G.; Neu, H. M.; Cantú Reinhard, F. G.; Goldberg, D. P.; de Visser, S. P. *J. Am. Chem. Soc*. **2016**, *138*, 12375–12386.

21. (a) de Visser, S. P. *Chem. Eur. J*. **2006**, *12*, 8168–8177. (b) Li, X.-X.; Postils, V.; Sun, W.; Faponle, A. S.; Solà, M.; Wang, Y.; Nam, W.; de Visser, S. P. *Chem. Eur. J*. **2017**, *23*, 6406–6418.

22. (a) Quesne, M. G.; Latifi, R.; Gonzalez-Ovalle, L. E.; Kumar, D.; de Visser, S. P. *Chem. Eur. J*. **2014**, *20*, 435–446. (b) Timmins, A.; Saint-André, M.; de Visser, S. P. *J. Am. Chem. Soc*. **2017**, *139*, 9855–9866.

23. (a) Groves, J. T.; Nemo, T. E. *J. Am. Chem. Soc*. **1983**, *105*, 6243-6248. (b) Rana, S.; Dey, A.; Maiti, D. *Chem. Commun*. **2015**, *51*, 14469 – 14472.

24. (a) Yoshizawa, K.; Kamachi, T.; Shiota, Y. *J. Am. Chem. Soc*. **2001**, *123*, 9806–9816. (b) Shaik, S.; Kumar, D.; de Visser, S. P.; Altun, A.; Thiel, W. *Chem. Rev*. **2005**, *105*, 2279–2328. (c) Shaik, S.; Kumar, D.; de Visser, S. P. *J. Am. Chem. Soc*. **2008**, *130*, 10128–10140. (d) Li, D.; Wang, Y.; Han, K. *Coord. Chem. Rev*. **2012**, *256*, 1137–1150.

25. (a) de Visser, S. P.; Kumar, D.; Cohen, S.; Shacham, R.; Shaik, S. *J. Am. Chem. Soc*. **2004**, *126*, 8362–8363. (b) Kumar, D.; Hirao, H.; Que Jr., L.; Shaik, S. *J. Am. Chem. Soc*. **2005**, *127*, 8026–8027. (c) Geng, C. Y.; Ye, S. F.; Neese, F. *Angew. Chem. Int. Ed*. **2010**, *49*, 5717–5720. (d) Srnec, M.; Solomon, E. I. *J. Am. Chem. Soc*. **2017**, *139*, 2396–2407.

26. Latifi, R.; Bagherzadeh, M.; de Visser, S. P. *Chem. Eur. J.* **2009**, *15*, 6651–6662.

27. Faponle, A. S.; Quesne, M. G.; Sastri, C. V.; Banse, F.; de Visser, S. P. *Chem. Eur. J*. **2015**, *21*, 1221–1236.

28. Faponle, A. S.; Banse, F.; de Visser, S. P. *J. Biol. Inorg. Chem*. **2016**, *21*, 453–462.

29. (a) Hernández-Ortega, A.; Quesne, M. G.; Bui, S.; Heyes, D. J.; Steiner, R. A.; Scrutton, N. S.; de Visser, S. P. *J. Am. Chem. Soc*. **2015**, *137*, 7474–7487. (b) Cantú Reinhard, F. G.; de Visser, S. P. *Chem. Eur. J.* **2017**, *23*, 2935–2944.

30. Shaik, S. *Phys. Chem. Chem. Phys*. **2010**, *12*, 8706–8720.

31. Cantú Reinhard, F. G.; Sainna, M. A.; Upadhyay, P.; Balan, G. A.; Kumar, D.; Fornarini, S.; Crestoni, M. E.; de Visser, S. P. *Chem. Eur. J.* **2016**, *22*, 18608–18619.

32. Faponle, A. S.; Quesne, M. G.; de Visser, S. P. *Chem. Eur. J*. **2016**, *22*, 5478–5483.

SYNOPSIS TOC (8.25x4.45 cm).